

different method on carbon-terminated SiC(000 $\bar{1}$) substrates (4), indicating a very low density of in-plane atomic scattering centers in those samples. Thus, the transport properties in epitaxial graphene are critically influenced by the microscopic properties of the sample, determined (at least) by the substrate and growth conditions. For carbon-based electronics, this work highlights the need for further microscopic studies that are correlated closely with macroscopic transport measurements.

References and Notes

- K. S. Novoselov *et al.*, *Nature* **438**, 197 (2005).
- Y. B. Zhang, Y. W. Tan, H. L. Stormer, P. Kim, *Nature* **438**, 201 (2005).
- E. McCann *et al.*, *Phys. Rev. Lett.* **97**, 146805 (2006).
- X. Wu *et al.*, *Phys. Rev. Lett.* **98**, 136801 (2007).
- A. K. Geim, K. S. Novoselov, *Nat. Mater.* **6**, 183 (2007).
- E. McCann, V. I. Fal'ko, *Phys. Rev. Lett.* **96**, 086805 (2006).
- T. Ohta *et al.*, *Science* **313**, 951 (2006).
- C. Berger *et al.*, *J. Phys. Chem. B* **108**, 19912 (2004).
- C. Berger *et al.*, *Science* **312**, 1191 (2006).
- E. Rollings *et al.*, *J. Phys. Chem. Solids* **67**, 2172 (2006).
- The identification of monolayer and bilayer graphene is made from counting the number of atomic steps from the SiC substrate layer combined with STS measurements. Layers are also differentiated by the appearance of Si adatom interface states visible on monolayer graphene (18).
- F. Owman, P. Martensson, *Surf. Sci.* **369**, 126 (1996).
- V. M. Pereira *et al.*, *Phys. Rev. Lett.* **96**, 036801 (2006).
- T. O. Wehling *et al.*, *Phys. Rev. B* **75**, 125425 (2007).
- H. A. Mizes, J. S. Foster, *Science* **244**, 559 (1989).
- K. F. Kelly, N. J. Halas, *Surf. Sci.* **416**, L1085 (1998).
- P. Ruffieux *et al.*, *Phys. Rev. Lett.* **84**, 4910 (2000).
- Additional text and data are available on Science Online.
- L. Petersen, P. Hofmann, E. W. Plummer, F. Besenbacher, *J. Electron Spectrosc. Relat. Phenom.* **109**, 97 (2000).
- J. E. Hoffman *et al.*, *Science* **297**, 1148 (2002).
- T. Ando, T. Nakanishi, R. Saito, *J. Phys. Soc. Jpn.* **67**, 2857 (1998).
- P. L. McEuen *et al.*, *Phys. Rev. Lett.* **83**, 5098 (1999).
- We thank M. Stiles, E. Jarvis, W. de Heer, X. Wu, C. Berger, and F. Guinea for valuable comments and discussions and S. Blankenship, F. Hess, A. Band, and N. Brown for their technical assistance. This work was supported in part by the Office of Naval Research, by Intel Research, and by NSF grant ECS-0404084.

Supporting Online Material

www.sciencemag.org/cgi/content/full/317/5835/219/DC1
Materials and Methods
Figs. S1 and S2
References

22 March 2007; accepted 22 May 2007
10.1126/science.1142882

Efficient Tandem Polymer Solar Cells Fabricated by All-Solution Processing

Jin Young Kim,^{1,2} Kwanghee Lee,^{1,2*} Nelson E. Coates,¹ Daniel Moses,¹ Thuc-Quyen Nguyen,¹ Mark Dante,¹ Alan J. Heeger¹

Tandem solar cells, in which two solar cells with different absorption characteristics are linked to use a wider range of the solar spectrum, were fabricated with each layer processed from solution with the use of bulk heterojunction materials comprising semiconducting polymers and fullerene derivatives. A transparent titanium oxide (TiO_x) layer separates and connects the front cell and the back cell. The TiO_x layer serves as an electron transport and collecting layer for the first cell and as a stable foundation that enables the fabrication of the second cell to complete the tandem cell architecture. We use an inverted structure with the low band-gap polymer-fullerene composite as the charge-separating layer in the front cell and the high band-gap polymer composite as that in the back cell. Power-conversion efficiencies of more than 6% were achieved at illuminations of 200 milliwatts per square centimeter.

Polymer solar cells based on conjugated polymer and fullerene composites offer special opportunities as renewable energy sources because they can be fabricated to extend over large areas by means of low-cost printing and coating technologies that can simultaneously pattern the active materials on lightweight flexible substrates (1–4). Although encouraging progress has been made with power-conversion efficiencies (η_c) of 5% having been reported (5–9), the limited efficiency has hindered the path toward commercialization.

The “tandem cell” architecture, a multilayer structure that is equivalent to two photovoltaic cells in series, offers a number of advantages. Because the two cells are in series, the open-circuit voltage (V_{oc}) is increased to the sum of the V_{oc} 's of the individual cells. The use of two semiconductors with different band gaps enables absorption over a broad range of photon energies

within the solar emission spectrum; the two cells typically use a wide band-gap semiconductor for the first cell and a smaller band-gap semiconductor for the second cell (10). Because the electron-hole pairs generated by photons with energies greater than that of the energy gap rapidly relax to the respective band edges, the power-conversion efficiency of the two cells in series is inherently better than that of a single cell made from the smaller band-gap material. Moreover, because of the low mobility of the charge carriers in the polymer-fullerene composites, an increase in the thickness of the active layer increases the internal resistance of the device, which reduces both the V_{oc} and fill factor (FF) (11). Thus, the tandem cell architecture can have a higher optical density over a wider fraction of the solar emission spectrum than that of a single cell without increasing the internal resistance. The tandem cell architecture can therefore improve the light harvesting in polymer-based photovoltaic cells.

Tandem structures have been investigated for small-molecule heterojunction organic solar cells (12–15) and for hybrid organic solar cells in which the first cell uses an evaporated small-molecule material and the second cell uses a conjugated polymer; the two cells are separated

by a semitransparent metal layer (16). Recently, polymer-fullerene composite tandem cells were reported (17–20). In these devices, a thermally evaporated metal layer is used as a charge-recombination layer and as a protection layer (to prevent interlayer mixing) during the spin-casting of the second cell (17–19). These polymer-based tandem cells exhibit a high V_{oc} , close to the expected sum of the V_{oc} 's of the two subcells, but the short-circuit current (J_{sc}) is lower than that of either single cell. When the same polymer was used for the front and back cells, the small J_{sc} was attributed to the absorption spectra being identical, so that the back cell absorbs less incident light and thus limits the photocurrent (because the two cells are in series, the current through the multilayer device is determined by that from the back cell). Moreover, because the interfacial metal layer is only semitransparent, the additional absorption also reduces the intensity of the light incident on the back cell. Thus, even when two different polymers are used, the photocurrent is correspondingly reduced.

We report here that we have successfully demonstrated the application of polymer-based bulk heterojunction tandem cells, with each layer processed from solution. A transparent TiO_x layer is used to separate and connect the front cell and the back cell. The TiO_x layer serves as an electron transport and collecting layer for the first cell and as a stable foundation that enables the fabrication of the second cell to complete the tandem cell architecture. In earlier work on tandem cells fabricated with organic semiconductors, the analogous intermediate layer was formed by the evaporative deposition of a semitransparent metal layer in high vacuum. This increases the complexity of device fabrication and causes unwanted loss of light intensity (due to absorption) to the back cell (14). For the tandem cells reported here, the TiO_x intermediate layer was deposited from solution (by means of sol-gel chemistry) with no substantial interlayer mixing. The performance of the polymer tandem solar cell is summarized as follows: $J_{sc} = 7.8 \text{ mA/cm}^2$, $V_{oc} = 1.24 \text{ V}$, $FF = 0.67$, and $\eta_c = 6.5\%$.

¹Center for Polymers and Organic Solids, University of California, Santa Barbara, CA 93106–5090, USA. ²Department of Materials Science and Engineering, Gwangju Institute of Science and Technology, Gwangju 500-712, Korea.

*To whom correspondence should be addressed. E-mail: klee@gist.ac.kr

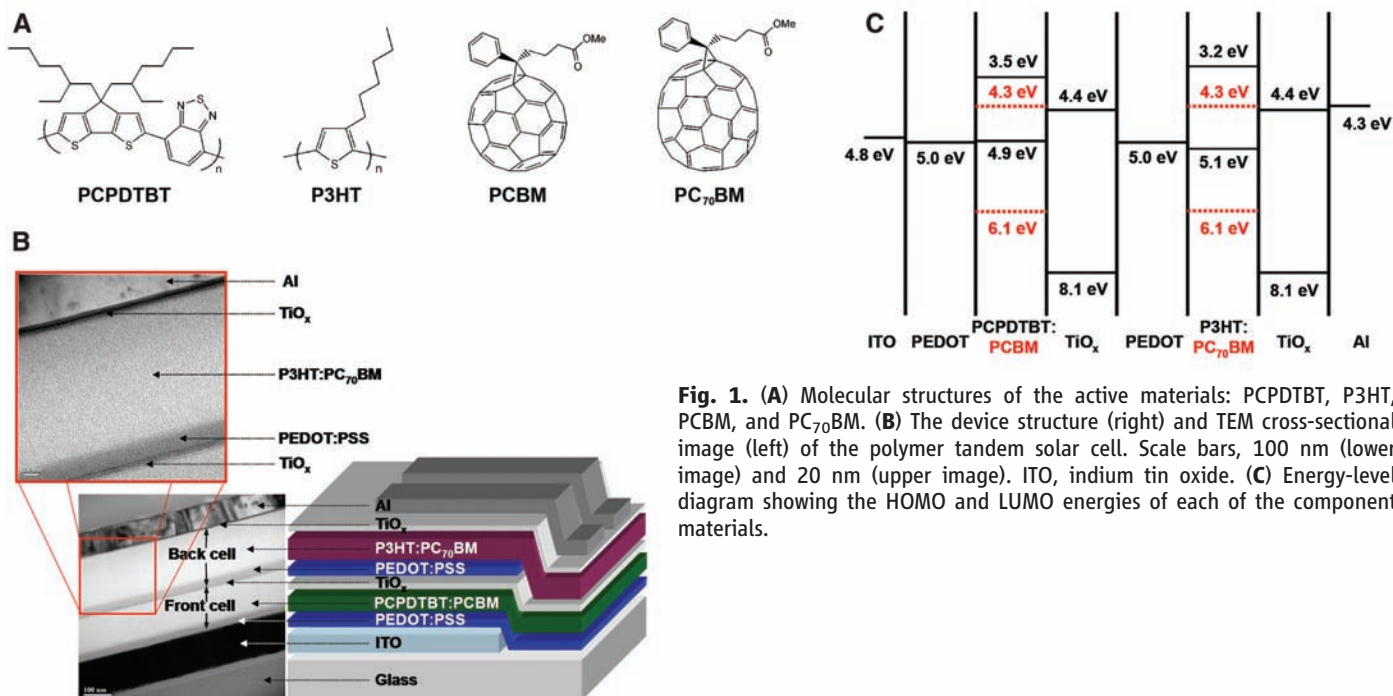


Fig. 1. (A) Molecular structures of the active materials: PCPDTBT, P3HT, PCBM, and PC₇₀BM. (B) The device structure (right) and TEM cross-sectional image (left) of the polymer tandem solar cell. Scale bars, 100 nm (lower image) and 20 nm (upper image). ITO, indium tin oxide. (C) Energy-level diagram showing the HOMO and LUMO energies of each of the component materials.

Figure 1 shows the structure of the multi-layer polymer tandem solar cell together with the chemical structure of its components. The charge-separation layer for the front cell is a bulk heterojunction composite of poly[2,6-(4,4-bis-(2-ethylhexyl)-4*H*-cyclopenta[2,1-*b*;3,4-*b'*]dithiophene)-*alt*-4,7-(2,1,3-benzothiadiazole)] (PCPDTBT) and [6,6]-phenyl-C₆₁ butyric acid methyl ester (PCBM). The charge-separation layer for the back cell is a bulk heterojunction composite of poly(3-hexylthiophene) (P3HT) and [6,6]-phenyl-C₇₁ butyric acid methyl ester (PC₇₀BM). The two polymer-fullerene layers are separated by a transparent TiO_x layer and a highly conductive hole transport layer, poly(3,4-ethylenedioxythiophene)-polystyrene sulfonic acid (PEDOT:PSS) (Baytron PH500 from H. C. Starck, Newton, Massachusetts, USA). Electrons from the first cell combine with holes from the second cell at the TiO_x-PEDOT:PSS interface.

The TiO_x layer is deposited by means of sol-gel chemistry, as described in (9). The TiO_x layer serves five separate functions. First, hydrophilic TiO_x separates the PEDOT:PSS that is cast on it from aqueous solution, from the underlying hydrophobic PCPDTBT:PCBM charge-separating layer of the front cell; the hydrophobic TiO_x precursor becomes hydrophilic after conversion to TiO_x. Second, the TiO_x layer breaks the symmetry in the front cell and thereby creates the open-circuit voltage. Third, the TiO_x functions as an electron transport layer. Fourth, the TiO_x functions as a hole blocking layer because the top of the valence band of TiO_x is sufficiently electronegative, 8.1 eV below the vacuum, to block holes (9). Finally, the top TiO_x layer (i.e., between the P3HT:PC₇₀BM charge-separating layer of the back cell and the aluminum elec-

trode) acts as an optical spacer that redistributes the light intensity to optimize the efficiency of the back cell (9).

Cross-sectional images of the polymer tandem solar cells taken with high-resolution transmission electron microscopy (TEM) show the individual layers clearly (Fig. 1B) (21). Perhaps more important, the various interfaces are very sharp; there is no interlayer mixing.

The energy-level diagram (Fig. 1C) indicates the highest occupied molecular orbital (HOMO) energies and the lowest unoccupied molecular orbital (LUMO) energies of the individual component materials. As noted, the V_{oc} of the tandem cell is equal to the sum of the V_{oc} of each subcell because the front and back cells are connected in series (12).

The absorption bands of the PCPDTBT and P3HT (Fig. 2A) complement each other and make these two materials appropriate for use in the two subcells of a spectrum-splitting tandem cell device. The absorption spectrum of a film of the bulk heterojunction composite of each subcell and that of a bilayer film of PCPDTBT:PCBM and P3HT:PC₇₀BM are shown in Fig. 2B. The absorption of the PCPDTBT:PCBM film is weak in the visible spectral range but has two strong bands: one in the near-infrared (near-IR) between 700 and 850 nm that arises from the interband π - π^* transition of the PCPDTBT (22) and one in the ultraviolet (UV) that arises primarily from the HOMO-LUMO transition of the PCBM. The absorption of the P3HT:PC₇₀BM film falls in the “hole” in the PCPDTBT:PCBM spectrum and covers the visible spectral range. The electronic absorption spectrum of the tandem structure can be described as a simple superposition of the absorption spectra of the two com-

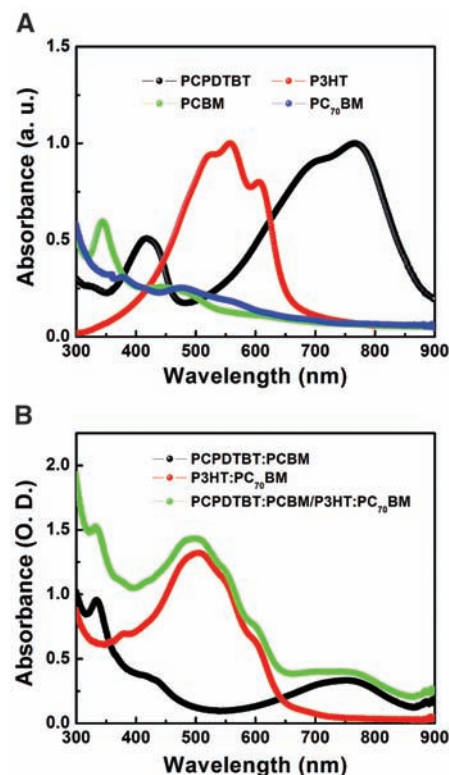


Fig. 2. (A) Absorption spectra of films of each material. The absorption band of the P3HT complements the absorption of PCPDTBT in visible range. a.u., arbitrary units. (B) Absorption spectra of a PCPDTBT:PCBM bulk heterojunction composite film, a P3HT:PC₇₀BM bulk heterojunction composite film, and a bilayer of the two as relevant to the tandem device structure. O.D., optical density.

plementary composites. Therefore, the PEDOT:PSS and TiO_x layers have negligible absorption in the tandem device structure.

Tandem cells generally use a wide band-gap material as the first charge-separation layer and a narrow band-gap material as the second charge-separation layer with a thinner front cell than the back cell so that the photocurrents generated in each subcell are balanced. In our case, because of the non-optimum phase morphology of the PCPDTBT:PCBM composite, increasing the film thickness of this layer above 130 nm leads to reduced values for both J_{sc} and FF in single cells (22). However, the J_{sc} of a P3HT:PC₇₀BM single cell increases as the film thickness increases up to 200 nm, beyond which the FF is reduced. Because of these material characteristics, we have chosen an “inverted tandem cell” structure with the low band-gap bulk heterojunction composite (PCPDTBT:PCBM) as the front cell and the higher band-gap bulk heterojunction composite (P3HT:PC₇₀BM) as the back cell (Fig. 1B) (21).

We have measured the incident photon-to-current collection efficiency (IPCE) spectra of both the single cells and of the tandem cell, using a bias light on the tandem cell to confirm

the series connection of the subcells and to extend the data over the full spectral coverage (Fig. 3A) (16, 21, 23). Each single cell shows the known spectral response of its bulk heterojunction composite, which is in excellent agreement with the absorption spectra of the two composites (Fig. 2B): The P3HT:PC₇₀BM composite gives a maximum IPCE of ~78% at 500 nm, and the PCPDTBT:PCBM composite has two dominant peaks (~35% at 750 to 800 nm and over 32% below 440 nm). When carrying out the measurements on the tandem cell, we find that biasing the device with 530-nm blue light and with 730-nm red light selectively excites the front and back cells, respectively, showing that (i) the device harvests photons from the UV to the near-IR, and (ii) each subcell functions individually (23).

The current density versus voltage (J - V) characteristics of single solar cells and the tandem solar cell with PCPDTBT:PCBM and P3HT:PC₇₀BM composites under Air Mass 1.5 Global (AM1.5G) illumination from a calibrated solar simulator with irradiation intensity of 100 mW/cm^2 are shown in Fig. 3B. The single devices show a typical photovoltaic response with device performance comparable to that reported in previ-

ous studies (9, 22); the PCPDTBT:PCBM single cell yields $J_{sc} = 9.2 \text{ mA}/\text{cm}^2$, $V_{oc} = 0.66 \text{ V}$, $FF = 0.50$, and $\eta_e = 3.0\%$, and the P3HT:PC₇₀BM single cell yields $J_{sc} = 10.8 \text{ mA}/\text{cm}^2$, $V_{oc} = 0.63 \text{ V}$, $FF = 0.69$, and $\eta_e = 4.7\%$.

With two subcells stacked in series, the current that is extracted from the tandem cell is determined by the current generated in either the front or back cell, whichever is smaller (23). Accordingly, when there is greater carrier generation in either subcell, these excess charges cannot contribute to the photocurrent and so compensate for the built-in potential across that subcell. This compensation leads to a reduced V_{oc} in the tandem cell (19).

To optimize and balance the current in each subcell, we tried all possible variations of the tandem cell architecture: by changing the order of the active materials, by varying the concentration and ratio of each component in the composite solutions, and by varying the thicknesses of the two bulk heterojunction materials. Because of the high extinction coefficient of the PCPDTBT:PCBM composite, the P3HT:PC₇₀BM back cell has the smaller J_{sc} of the two subcells and is thus the limiting cell (23). The FF of the

Fig. 3. (A) IPCE spectra of single cells and a tandem cell with bias light. We carried out the IPCE measurements using modulation spectroscopy with a lock-in amplifier for the single cells and for the tandem cell without light bias. For the tandem cell measurements made with bias light, unmodulated monochromatic light with an intensity of ~2 mW/cm^2 was used. **(B)** J - V characteristics of single cells and tandem cell with PCPDTBT:PCBM and P3HT:PC₇₀BM composites under AM1.5G illumination from a calibrated solar simulator with irradiation intensity of 100 mW/cm^2 (about one sun) are presented. The power-conversion efficiency of a solar cell is given as $\eta_e = (J_{sc} \cdot V_{oc} \cdot FF) \cdot 100 / P_{inc}$, where P_{inc} is the intensity of incident light. The device performance is summarized as follows: The PCPDTBT:PCBM single cell shows $J_{sc} = 9.2 \text{ mA}/\text{cm}^2$, $V_{oc} = 0.66 \text{ V}$, $FF = 0.50$, and $\eta_e = 3.0\%$; the P3HT:PC₇₀BM single cell shows $J_{sc} = 10.8 \text{ mA}/\text{cm}^2$, $V_{oc} = 0.63 \text{ V}$, $FF = 0.69$, and $\eta_e = 4.7\%$; and the tandem cell shows $J_{sc} = 7.8 \text{ mA}/\text{cm}^2$, $V_{oc} = 1.24 \text{ V}$, $FF = 0.67$, and $\eta_e = 6.5\%$.

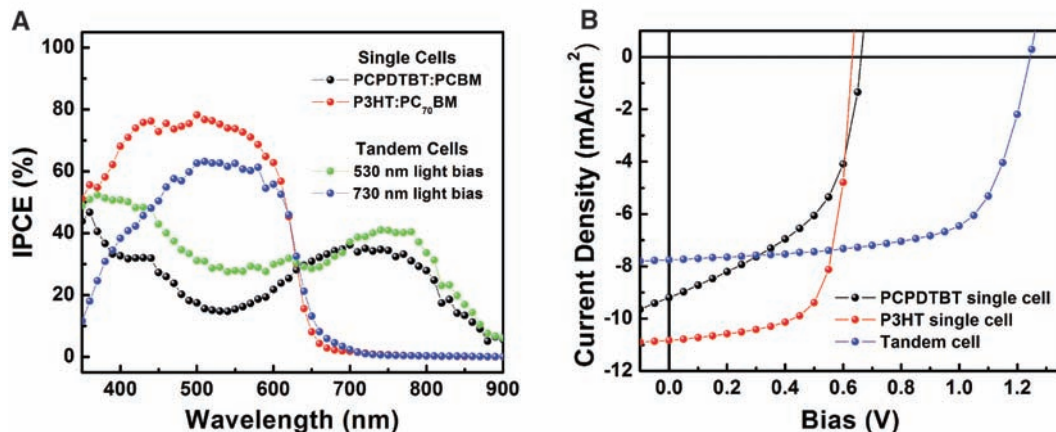
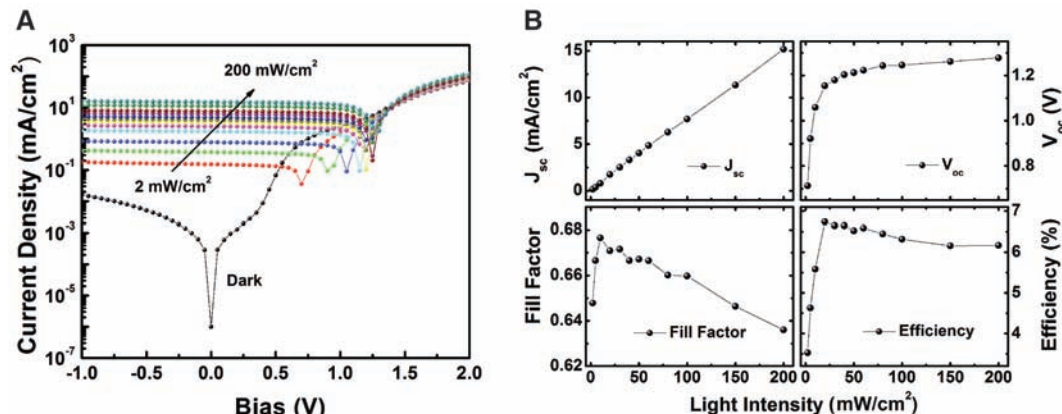


Fig. 4. (A) J - V characteristics of the optimized tandem cell measured with different incident light intensities from 0 to 200 mW/cm^2 (AM1.5G solar spectrum). **(B)** J_{sc} , V_{oc} , FF , and η_e of the tandem cell are plotted as functions of the incident light intensities. The η_e of the optimized tandem cell reaches its maximum of $\eta_e = 6.7\%$ at 20 mW/cm^2 .



tandem cell can be very near the FF of the limiting cell. Thus, we use the P3HT:PC₇₀BM as the back cell to obtain a higher FF .

More than 200 individual tandem cells were made in order to optimize the fabrication procedure and device architecture (24). This optimization led to the inverted tandem cell device depicted in Fig. 1B. Using this inverted structure, we fabricated more than 20 tandem cells with efficiencies above 6.2%. Performance parameters for a typical device are as follows: $J_{sc} = 7.8 \text{ mA/cm}^2$, $V_{oc} = 1.24 \text{ V}$, $FF = 0.67$, and $\eta_e = 6.5\%$. The J_{sc} in the tandem cell is consistent with the IPCE measurements because the photocurrent in the back cell from IPCE is 72% of that of the P3HT:PC₇₀BM single cell, confirming that the back cell is the limiting cell for J_{sc} as well as for FF .

Initial measurements of the stability of the tandem cell yield promising results. After storing the tandem cell in N₂ for 3500 hours (fig. S2A), its efficiency decreased from $\eta_e = 6.5$ to 5.5%. This relatively small decrease after nearly half a year confirms the robustness of the tandem cell architecture. Moreover, the tandem solar cells showed reasonable stability under continuous illumination. When exposed continuously to irradiation with an intensity of one sun (AM1.5G), the tandem cell retained ~70% of its original efficiency after 40 hours and over 60% even after 100 hours (fig. S2B) (21). Clearly, more extensive measurements on the degradation of packaged devices are required in future work.

The J - V characteristics of the optimized inverted tandem cell, measured with different

incident light intensity from 0 to 200 mW/cm², are shown in Fig. 4A. In Fig. 4B, the performance parameters of the tandem cell (J_{sc} , V_{oc} , FF , and η_e) are plotted as functions of the incident light intensity. Because J_{sc} is linear with illuminated light intensity, there is no substantial space charge buildup in the tandem device. The V_{oc} also increases monotonically with an increase in the light intensity and approaches 1.3 V under AM1.5G conditions at 200 mW/cm², the sum of V_{oc} of the two subcells. The FF approaches 0.68 at 10 mW/cm², a value near the FF of the limiting P3HT:PC₇₀BM back cell, and exceeds 0.63 at 200 mW/cm². The power-conversion efficiency of the optimized tandem cell reaches its maximum of $\eta_e = 6.7\%$ at 20 mW/cm², whereas $\eta_e = 3.5\%$ at 2 mW/cm² and $\eta_e = 6.1\%$ at 200 mW/cm². With these performance parameters, it is evident that the subcells in our tandem cell are connected in series and provide enhanced coverage of the solar spectrum.

References and Notes

- N. S. Sariciftci, L. Smilowitz, A. J. Heeger, F. Wudl, *Science* **258**, 1474 (1992).
- G. Yu, J. Gao, J. C. Hemmelen, F. Wudl, A. J. Heeger, *Science* **270**, 1789 (1995).
- C. J. Brabec, *Sol. Energy Mater. Sol. Cells* **83**, 273 (2004).
- K. M. Coakley, M. D. McGehee, *Chem. Mater.* **16**, 4533 (2004).
- W. Ma, C. Y. Yang, X. Gong, K. Lee, A. J. Heeger, *Adv. Funct. Mater.* **15**, 1617 (2005).
- M. Reyes-Reyes, K. Kim, D. L. Carroll, *Appl. Phys. Lett.* **87**, 083506 (2005).
- G. Li *et al.*, *Nat. Mater.* **4**, 864 (2005).
- Y. Kim *et al.*, *Nat. Mater.* **5**, 197 (2006).
- J. Y. Kim *et al.*, *Adv. Mater.* **18**, 572 (2006).
- M. W. Wanlass *et al.*, *Sol. Cells* **27**, 191 (1989).
- I. Riedel, V. Dyakonov, *Phys. Status Solidi A* **201**, 1332 (2004).
- M. Hiramoto, M. Suezaki, M. Yokoyama, *Chem. Lett. (Jpn.)* **19**, 327 (1990).
- A. Yakimov, S. R. Forrest, *Appl. Phys. Lett.* **80**, 1667 (2002).
- J. Xue, S. Uchida, B. P. Rand, S. R. Forrest, *Appl. Phys. Lett.* **85**, 5757 (2004).
- J. Drechsel *et al.*, *Appl. Phys. Lett.* **86**, 244102 (2005).
- G. Dennler *et al.*, *Appl. Phys. Lett.* **89**, 073502 (2006).
- V. Shrotriya, E. H.-E. Wu, G. Li, Y. Yao, Y. Yang, *Appl. Phys. Lett.* **88**, 064104 (2006).
- K. Kawano, N. Ito, T. Nishimori, J. Sakai, *Appl. Phys. Lett.* **88**, 073514 (2006).
- A. Hadjipour *et al.*, *Adv. Funct. Mater.* **16**, 1897 (2006).
- J. Gilot, M. M. Wienk, R. A. J. Janssen, *Appl. Phys. Lett.* **90**, 143512 (2007).
- Materials and methods are available as supporting material on Science Online.
- D. Mühlbacher *et al.*, *Adv. Mater.* **18**, 2884 (2006).
- J. Burdick, T. Glatfelter, *Sol. Cells* **18**, 301 (1986).
- All the solar cell devices were fabricated by J.Y.K., who also measured their performance. The IPCE measurements were performed by J.Y.K. and N.E.C. The TEM images were obtained by M.D.
- The research was supported by Konarka Technologies (Lowell, MA), by the U.S. Department of Energy (under grant DE-FG02-06ER46324), and by the Ministry of Science & Technology of Korea under the International Cooperation Research Program (Global Research Laboratory Program: K.L. and A.J.H., Principal Investigators). The PCPDTBT, PCBM, P3HT, and PC₇₀BM materials were supplied for our use by Konarka Technologies. We thank W. Ma for contributions during the early phase of this work.

Supporting Online Material

www.sciencemag.org/cgi/content/full/317/5835/222/DC1
Materials and Methods
Figs. S1 and S2
References

23 February 2007; accepted 16 May 2007
10.1126/science.1141711

Cleaving Mercury-Alkyl Bonds: A Functional Model for Mercury Detoxification by *MerB*

Jonathan G. Melnick and Gerard Parkin*

The extreme toxicity of organomercury compounds that are found in the environment has focused attention on the mechanisms of action of bacterial remediating enzymes. We describe facile room-temperature protolytic cleavage by a thiol of the Hg-C bond in mercury-alkyl compounds that emulate the structure and function of the organomercurial lyase *MerB*. Specifically, the tris(2-mercapto-1-*t*-butylimidazolyl)hydroborato ligand [Tm^{Bu}], which features three sulfur donors, has been used to synthesize [Tm^{Bu}]HgR alkyl compounds (R = methyl or ethyl) that react with phenylthiol (PhSH) to yield [Tm^{Bu}]HgSPh and RH. Although [Tm^{Bu}]HgR compounds exist as linear two-coordinate complexes in the solid state, ¹H nuclear magnetic resonance spectroscopy indicates that the complexes exist in rapid equilibrium with their higher-coordinate [κ²-Tm^{Bu}]HgR and [κ³-Tm^{Bu}]HgR isomers in solution. Facile access to a higher-coordinate species is proposed to account for the exceptional reactivity of [Tm^{Bu}]HgR relative to that of other two-coordinate mercury-alkyl compounds.

The extreme toxicological problems associated with mercury and its compounds (1) are largely a consequence of the high affinity of mercury for sulfur. As such, mercury binds readily to the thiol groups of cysteine residues in proteins and enzymes and may displace

Zn(II) from cysteine-rich structural and catalytic zinc sites (2). For example, Hg(II) inhibits the Fpg DNA repair protein by a mechanism that is believed to involve replacement of Zn(II) in the Cys₄ zinc finger binding site (3–6). Mercury alkyls, in particular, are potent neurotoxins be-

cause they bind so strongly to protein residues and are capable of crossing the blood-brain barrier. Indeed, methyl-mercury compounds are responsible for Minamata disease, so-called because it caused the death of almost 2000 people around Minamata Bay (Japan) in the late 1950s when the residents consumed fish that was contaminated with methyl-mercury compounds (1). Although the initial outbreak of the disease was a result of toxic release from a nearby chemical plant, methyl-mercury compounds are also introduced into the environment by biomethylation of naturally occurring Hg(II) in an aquatic environment (7, 8). The Hg-CH₃ bond is kinetically stable toward protolytic cleavage in aqueous solution, with the result that methyl-mercury compounds accumulate in predatory fish and may be consumed by humans (1, 7).

Detoxification of organomercury compounds is therefore of critical importance. In nature, this is achieved by the combined action of two enzymes. Specifically, bacterial organomercurial lyase (*MerB*) achieves protolytic cleavage of the

Department of Chemistry, Columbia University, New York, NY 10027, USA.

*To whom correspondence should be addressed. E-mail: parkin@columbia.edu